Available online at www.sciencedirect.com
ScienceDirect
Journal of Magnetic Resonance 187 (2007) 277–287
JMR Journal of Magnetic Resonance
www.elsevier.com/locate/jmr

Uniform distribution of projection data for improved reconstruction quality of 4D EPR imaging

Rizwan Ahmad [a,b], Deepti S. Vikram [a], Bradley Clymer [b,c], Lee C. Potter [b], Yuanmu Deng [a], Parthasarathy Srinivasan [d], Jay L. Zweier [a], Periannan Kuppusamy [a,*]

[a] Center for Biomedical EPR Spectroscopy and Imaging, Davis Heart and Lung Research Institute, Department of Internal Medicine, The Ohio State University, 420 West 12th Avenue, Room 114, Columbus, OH 43210, USA
[b] Department of Electrical and Computer Engineering, The Ohio State University, Columbus, OH 43210, USA
[c] Department of Biomedical Engineering, The Ohio State University, Columbus, OH 43210, USA
[d] Mathematical Biosciences Institute, The Ohio State University, Columbus, OH 43210, USA

Received 18 March 2007; revised 10 May 2007
Available online 25 May 2007

Abstract

In continuous wave (CW) electron paramagnetic resonance imaging (EPRI), high quality of reconstruction in a limited acquisition time is a high priority. It has been shown for the case of 3D EPRI, that a uniform distribution of the projection data generally enhances reconstruction quality. In this work, we have suggested two data acquisition techniques for which the gradient orientations are more evenly distributed over the 4D acquisition space as compared to the existing methods. The first sampling technique is based on equal solid angle partitioning of 4D space, while the second technique is based on Fekete points estimation in 4D to generate a more uniform distribution of data. After acquisition, filtered backprojection (FBP) is applied to carryout the reconstruction in a single stage. The single-stage reconstruction improves the spatial resolution by eliminating the necessity of data interpolation in multi-stage reconstructions. For the proposed data distributions, the simulations and experimental results indicate a higher fidelity to the true object configuration. Using the uniform distribution, we expect about 50% reduction in the acquisition time over the traditional method of equal linear angle acquisition.

Keywords: 4D inverse Radon transform; Fekete points; Reconstruction artifacts; EPRI; Single-stage reconstruction

1. Introduction

Electron paramagnetic resonance imaging (EPRI) is a noninvasive technique that is capable of detecting and imaging free radicals [1]. Due to its ability for direct detection and characterization of both endogenous and introduced free radicals, EPRI has a distinct advantage in many biological applications [2–7]. However, the long acquisition time, especially for 4D spectral-spatial imaging, can be a bottle-neck for many *in vivo* biological applications. It has been shown for the 3D case [8] that uniformity of the data distribution can improve the reconstruction quality for a given acquisition time. In this work, we investigate uniform data distributions and their impact on 4D spectral-spatial imaging.

Most of the EPR experiments are conducted in continuous wave (CW) domain since the technical challenges associated with the pulsed EPR [9] limit its broad use. In CW EPRI, the data are acquired in the form of projections [10], and filtered backprojection (FBP) [11] or Fourier-based direct reconstruction techniques [12] are commonly applied to reconstruct the image from the acquired projections. The quality of the reconstructed image depends on a number of factors including number of acquired projections, signal-to-noise ratio (SNR), field homogeneity,

* Corresponding author. Fax: +1 614 292 8454.
E-mail address: kuppusamy.1@osu.edu (P. Kuppusamy).

1090-7807/$ - see front matter © 2007 Elsevier Inc. All rights reserved.
doi:10.1016/j.jmr.2007.05.012

linewidth of the paramagnetic species under study, and the reconstruction technique itself. Generally, the reconstruction quality can be improved by acquiring more projections. This, however, is not a viable solution because projection acquisition can be a time-consuming process [13]. Hence, increasing the number of acquired projections beyond a certain limit may not be practical, especially for *in vivo* biological applications. Hence, it is highly desirable to improve the reconstruction quality from a limited number of projections.

The EPRI can be performed in purely spatial domain to obtain one-, two-, or three-dimensional (1D, 2D, or 3D) images of free radical distribution in objects. It is important to mention that purely spatial 3D EPRI provides unambiguous distribution of free radicals under the assumption that spectral shape is space-invariant. Thus, for samples having variable linewidths or multiple radical species, it is not possible to obtain an accurate map of the spin distribution using purely spatial EPRI. Besides, the information obtained by purely spatial EPRI is limited to the spin density and not the nature of the spins at each spatial volume element (voxel). To overcome this limitation an additional dimension, the spectral dimension, is required to capture the spectral shape function at each voxel. The imaging technique that includes a spectral dimension along with one or more spatial dimensions is termed as spectral-spatial imaging [14]. While the spatial information is captured by collecting projections along different orientations of the gradient vector, the spectral information is encoded by varying the gradient strength. The spectral-spatial imaging can be performed in 1, 2 or 3 spatial dimensions giving rise to 2, 3, or 4D spectral-spatial images, respectively. While the information provided by the additional spectral dimension is immensely useful in many biological applications, it requires additional hardware capability, manageable experimental conditions, and additional acquisition time. The potential application of the spectral-spatial technique has been recognized in performing EPRI oximetry [15] that is based on the effect of oxygen-induced broadening of the lineshape.

It is beneficial to take advantage of any symmetry or redundancy in the object configuration to reduce the number of acquired projections. A few adaptive acquisition techniques have been presented [8,16] where a more informative set of projections is acquired. This strategy is advantageous only where the object configuration is highly anisotropic in a way that the information depicted in a small number of projections is sufficient to reasonably characterize the object configuration. In cases where the object does not possess any exploitable configuration or there is not enough information available about the object configuration, an uniform sampling of the data over the object space generates consistent results. Equal solid angle (ESA)-based sampling for 3D EPRI has been presented earlier [8] which results in an estimated reduction of 30% in the acquisition time over equal linear angle (ELA)-based sampling. A further improvement in the reconstruction has been observed [17] by obtaining a more uniform distribution of the gradient.

Although ESA-based distribution designed for 3D has been applied to 4D imaging [18], the resulting distribution has an improved uniformity only in the 3D spatial domain and the overall sampling in 4D domain is still not uniform. In addition, since the set of selected gradient orientations is identical for each applied gradient strength, there is a high redundancy in the collected data. The first technique presented here is an extension of the 3D ESA-based distribution [19] while the second proposed technique is an estimation of Fekete points [20] in 4D which generally results in more uniform distribution of the data. We expect about 50% reduction in the acquisition time over ELA-based distribution and about 25% reduction over the previously proposed sampling technique where ESA approximation holds only in the 3D spatial domain [18]. Since the reconstruction is carried out in a single stage without the necessity of interpolation, the spatial resolution does not degrade. The computation time, however, can be longer as compared to multistage reconstruction where nD EPR image is reconstructed through $(n-1)$ stages of 2D back-projection operations [21]. By limiting the size of the reconstructed image and by breaking the reconstruction into subsets, the processing time for 4D single-stage reconstruction can be deemed manageable.

2. Theory

In CW EPRI, a projection is generally acquired by measuring the absorption signal as a function of magnetic field in the presence of a static gradient. The orientation of the acquired projection is determined by the direction of the magnetic field gradient which is a vector sum of three independent and mutually orthogonal field gradients in the x, y, and z directions. In 4D, Radon transform [21] of an object $f(x,y,z,s)$ is expressed as

$$p(\rho,\eta,\phi,\theta) = \int_{-\infty}^{\infty}\int_{-\infty}^{\infty}\int_{-\infty}^{\infty}\int_{-\infty}^{\infty} f(x,y,z,s) \times \delta(x\cos\eta\sin\phi\sin\theta + y\sin\eta\sin\phi\sin\theta + z\cos\phi\sin\theta + s\cos\theta - \rho)\,\mathrm{d}x\mathrm{d}y\mathrm{d}z\mathrm{d}s \quad (1)$$

where ρ defines the distance of a particular line of integration from the origin, θ represents the spectral angle defined by Eq. (2), angles ϕ (90° − elevation) and η (azimuth) define the 3D spatial domain, and $p(\rho,\eta,\phi,\theta)$ represents an acquired projection along the orientation defined by hyperspherical coordinates η, ϕ, and θ. The distribution of η, ϕ, and θ determines the distribution of projection data in 4D space.

$$\tan\theta = G\frac{\Delta L}{\Delta B} \quad (2)$$

where G is the gradient strength, ΔL and ΔB are spatial field of view (FOV) and spectral window, respectively.

Once a sufficient number of projections are acquired, the image can be reconstructed by the FBP method which is

based on the inverse Radon transform. The FBP method requires that the gradient orientations for the projection data are uniformly distributed over the acquisition space that, for 4D EPRI, is simply S^3 which is defined as

$$S^d := \{\vec{r} \in \mathbb{R}^{d+1} \mid \vec{r} \cdot \vec{r} = 1\} \tag{3}$$

where "$\cdot$" represents inner product on $\mathbb{R}^{d+1}$.

If the projections are not uniformly distributed, an appropriate weighting can be used to satisfy the requirement of the FBP

$$\begin{aligned} f(x,y,z,s) = \int_0^{\pi}\int_0^{\pi}\int_0^{\pi} p_{\mathrm{f}}(&x\cos\eta\sin\phi\sin\theta \\ &+ y\sin\eta\sin\phi\sin\theta + z\cos\phi\sin\theta \\ &+ s\cos\theta,\eta,\phi,\theta)(\sin\phi\sin^2\theta)\mathrm{d}\eta\mathrm{d}\phi\mathrm{d}\theta \end{aligned} \tag{4}$$

where p_{f} represents filtered projection.

$$p_{\mathrm{f}}(\rho,\eta,\phi,\theta) = \mathrm{IFT}(P(\rho,\eta,\phi,\theta) \mid v|^3) \tag{5}$$

where IFT stands for the inverse Fourier transform, P represents the Fourier transform (FT) of projection p, and v represents radial distance from the origin of Fourier domain. See Appendix A for derivation of Eqs. (4) and (5). For a limited number of projections N, Eq. (4) can be approximated numerically by selecting a suitable distribution of sampling points.

$$\begin{aligned} \tilde{f}(x,y,z,s) = \frac{1}{N}\sum_{i=1}^{N} &p_{\mathrm{f}}(x\cos\eta_i\sin\phi_i\sin\theta_i + y\sin\eta_i \\ &\times \sin\phi_i\sin\theta_i + z\cos\phi_i\sin\theta_i + s \\ &\times \cos\theta_i,\eta_i,\phi_i,\theta_i)\cdot w_i \end{aligned} \tag{6}$$

where w_i the weight associated with the ith projection, and its value depends on the data distribution. The error of approximation $(f-\tilde{f})$ depends on the number of projections (N) and the distribution of the projections. Generally, a projection distribution which is more uniform over the sphere (hypersphere) results in smaller approximation errors because there is a connection between better uniformity of data distribution and more accurate integration [22].

2.1. Equal linear angle sampling in 4D (ELA4)

In the traditional acquisition technique, the projection angles η, ϕ, and θ are sampled at a constant interval as shown in Fig. 1a. The reconstruction from a limited number of such projections is described by Eq. (7).

$$\begin{aligned} \tilde{f}(x,y,z,s) = \frac{1}{M^3}\sum_{m=1}^{M}\sin^2(m\Delta\theta)\sum_{n=1}^{M}\sin(n\Delta\phi) \\ \times\sum_{k=1}^{M} p_{\mathrm{f}}(x\cos(k\Delta\eta)\sin(n\Delta\phi)\sin(m\Delta\theta) \\ + y\sin(k\Delta\eta)\sin(n\Delta\phi)\sin(m\Delta\theta) + z\cos(n\Delta\phi) \\ \times\sin(m\Delta\theta) + s\cos(m\Delta\theta), k\Delta\eta, n\Delta\phi, m\Delta\theta) \end{aligned} \tag{7}$$

where M is the number of projections corresponding to $\theta = 90°$, $\phi = 90°$. An equal increment of η, ϕ, and θ results in a nonuniform distribution of the data over S^3. The acquired data becomes highly concentrated when ϕ or θ approaches 0° or 180°. The weighting term $\sin^2(m\Delta\theta)\sin(n\Delta\phi)$ in Eq. (7) effectively compensates for the nonuniformity of the data, but nevertheless reduces the acquisition efficiency. In addition, the sampling of data on a rigid latitude–longitude grid can lead to more pronounced reconstruction artifacts, because in such cases streak-artifact from various projections, if they get aligned to an edge of the object, may get added constructively.

2.2. Equal solid angle sampling in spatial domain (ESA3)

A distribution based on ESA approximation in S^2, applied to S^3, is shown in Fig. 1b. In the 3D spatial domain, the solid angle associated with gradient orientation is proportional to $\Delta\phi\Delta\eta\sin\phi$, and the ESA span [19] can be approximated by keeping $\Delta\phi$ constant and incrementing $\Delta\eta$ in proportion to $1/\sin\phi$. This way, the number of azimuth samples for each ϕ is determined as

$$K_n = \mathrm{round}(M\sin(n\Delta\phi)) \tag{8}$$

Therefore, as ϕ changes, the number of points also changes accordingly, which results in a more uniform distribution of the gradient directions over S^2 representing the spatial domain. Consequently, for ESA3 Eq. (7) can be modified as

$$\begin{aligned} \tilde{f}(x,y,z,s) = \frac{1}{M^2}\sum_{m=1}^{M}\sin^2(m\Delta\theta)\sum_{n=1}^{M}\frac{\sin(n\Delta\phi)}{K_n} \\ \times\sum_{k=1}^{K_n} p_{\mathrm{f}}(x\cos(\eta_k)\sin(n\Delta\phi)\sin(m\Delta\theta) \\ + y\sin(\eta_k)\sin(n\Delta\phi)\sin(m\Delta\theta) + z\cos(n\Delta\phi) \\ \times\sin(m\Delta\theta) + s\cos(m\Delta\theta), \eta_k, n\Delta\phi, m\Delta\theta) \end{aligned} \tag{9}$$

Since $\sin(n\Delta\phi)/K_n \approx 1/M$, it is evident from Eq. (9) that all the projections are weighted approximately by $\sin^2(m\Delta\theta)$ instead of $\sin^2(m\Delta\theta)\sin(n\Delta\phi)$ as was for ELA4. This weighting reflects a distribution that avoids nonuniformity around $\phi = 0°$ or $\phi = 180°$ but still suffers from data congestion around $\theta = 0°$ or $\theta = 180°$. In other words, the data from the resulting sampling pattern is crowded for lower gradient strengths and sparse for higher gradient strengths. The reconstruction results for 4D EPRI using ESA3 based distributions has been reported recently [18].

2.3. Equal solid angle sampling in 4D (ESA4)

In S^3, the solid angle associated with the gradient orientation is proportional to $\Delta\theta\Delta\phi\Delta\eta\sin^2\theta\sin\phi$ which can be computed from the Jacobian of the transformation (between hyperspherical and Cartesian coordinate systems) equations. The equal solid angle span for S^3 can be approximated by keeping $\Delta\theta$ constant and incrementing $\Delta\phi$ in

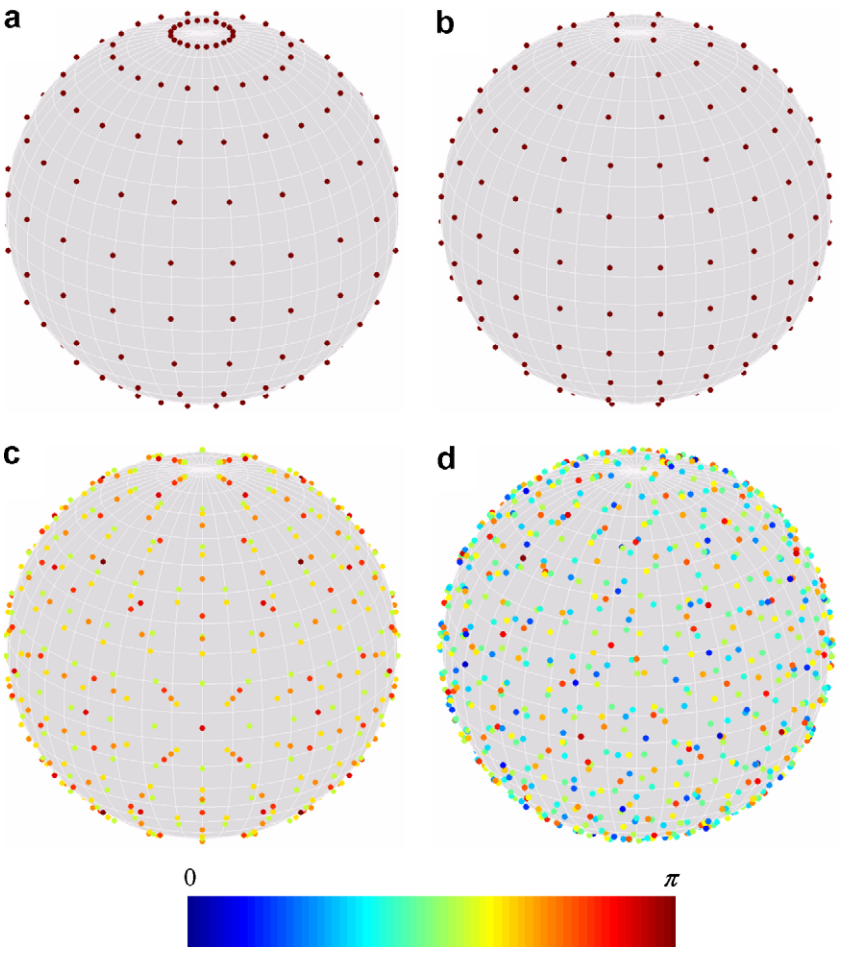

Fig. 1. The distribution of data points in 4D spectral-spatial domain. The dots locations on the sphere represent the gradient orientation in the spatial domain while the color represents the spectral angle. (a) Thousand data points (along with the antipodal points) generated using equal linear angle (ELA4) acquisition. Here, $\Delta\theta = \Delta\phi = \Delta\eta$=18°. (b) Eleven hundred fifty-two data points generated using equal solid angle in 3D (ESA3). Here, $\Delta\theta = \Delta\phi$=15°, and $\Delta\eta$ is varied in proportion to $1/\sin\phi$. (c) Six hundred sixty-four data points generated by equal solid angle in 4D (ESA4). Here, $\Delta\theta = 12.8°$, $\Delta\phi$ is varied in proportion to $1/\sin\theta$ and $\Delta\eta$ is $1/(\sin\phi\sin\theta)$. (d) Six hundred five data points with the uniform distribution defined by Fekete points (UF4). For ELA4 and ESA3, since the data distribution over spatial domain (defined by η and ϕ) is replicated for all selected values of θ, the dots of different colors overlap at each spatial location. Therefore, only red dots are visible for (a) and (b). For ESA4 shown in (c), the data distributions over spatial domain for $m\Delta\ \theta$ and $180° - m\Delta\theta$ are identical. Therefore, the data residing only in the second half of θ are visible. (For interpretation of the references in color in this figure legend, the reader is referred to the web version of this article.)

proportion to $1/\sin\theta$ and incrementing $\Delta\eta$ in proportion to $1/(\sin\theta\sin\phi)$. This way, the number of samples along ϕ and η are, respectively, determined as

$$J_m = \text{round}(M\sin(m\Delta\theta)) \tag{10}$$

$$K_j = \text{round}(J_m\sin(\phi_j)) \tag{11}$$

where $\phi_j = j(180°/J_m)$. The reconstruction from 4D equal solid angle acquisition is represented as

$$\begin{aligned}\tilde{f}(x,y,z,s) = \frac{1}{M}\sum_{m=1}^{M}\frac{\sin(m\Delta\theta)}{J_m}\sum_{j=1}^{J_m}\frac{\sin(m\Delta\theta)\sin(\phi_j)}{K_j} \\ \times\sum_{k=1}^{K_j}p_f(x\cos(\eta_k)\sin(\phi_j)\sin(m\Delta\theta)+y\sin(\eta_k) \\ \times\sin(\phi_j)\sin(m\Delta\theta)+z\cos(\phi_j)\sin(m\Delta\theta) \\ +s\cos(m\Delta\theta),\eta_k,\phi_j,m\Delta\theta)\end{aligned} \tag{12}$$

This distribution avoids concentrating data when ϕ or θ approaches 0° or 180° and hence improves the overall uniformity of data in S^3. A distribution based on ESA4 in shown in Fig. 1c.

Since projections corresponding to higher gradient have lower SNR, it is a common practice to spend more acquisition time for those projections to partially improve their SNR. If the acquisition time of a projection is made proportional to $1/\cos\theta$, the additional percentage reduction R in the acquisition time associated with ESA4 is

$$R = \left(1 - \frac{\sum_{m=1}^{M}\sin^2(m\Delta\theta - \Delta\theta/2)/|\cos(m\Delta\theta - \Delta\theta/2)|}{\sum_{m=1}^{M}1/|\cos(m\Delta\theta - \Delta\theta/2)|}\right)\times 100 \tag{13}$$

where

$$\Delta\theta = \frac{180^\circ}{M} \tag{14}$$

The value of R for $M = 18$ (with missing angle region 85°–95°) is 23% and for $M = 10$ (with missing angle of 81°–99°) is 26%. These savings are in addition to the 30% savings offered by ESA3 method [18]. As a result, net savings offered by ESA4 over ELA4 for $M = 18$ and $M = 10$ are 46% and 48%, respectively.

2.4. Uniform sampling based in Fekete points in 4D (UF4)

The problem of uniformly distributing a large number of points over S^2 has been studied extensively [20,23–25]. Several studies have suggested methods for efficient powder averaging [26] where a discrete set of crystallite orientations are used to simulate the NMR spectra. Bak et al. [27] has numerically analyzed the performances of various powder averaging methods to compare their insensitivities to the orientation of the object from which the spectra is observed and reported that the performance of so called REPULSION technique, which is similar to the one presented here, is on par or superior to the other popular techniques. More importantly, most of these other methods are only valid for S^2 and their extension to S^3 is not obvious, which is also the case for the distribution based on two successive Fibonacci numbers, whose feasibility for 3D spatial EPRI has been recently reported [17]. In recent years, spherical designs [28] have received a great deal of attention because they generate optimal distributions (in terms of zero integration error) for any integrand that can be approximated by a polynomial of limited degree. For EPRI, however, a direct application of most of these methods is prohibited since they do not offer the flexibility to account for additional restrictions such as antipodal symmetry, missing angle regions, and a large number of data points to be distributed. Another popular way to generate uniform distributions is via optimization with respect to a suitable criterion such as generalized energy [29], and the bounds on the corresponding separation radius, star discrepancy [30], and integration error have also been reported [31,32]. The main advantage of this approach for 4D spectral-spatial EPRI is its ability to accommodate the above mentioned EPRI related constraints. The energy U for a distribution $x_1, x_2, \ldots, x_N$ is defined as

$$U(t, \omega_N) = \frac{1}{2} \sum_{1 \leqslant j < k < N} |x_j - x_k|^{-t} \tag{15}$$

The objective to find ω_N that denotes a generic subset of S^2 (or S^3 in our case) with N elements $x_1^*, x_2^*, \ldots, x_N^*$ for which energy U is minimized. For $t = 1$, this represents the electrostatic potential energy of N charged particles that repel each other according to the Coulomb's law. Such points are called Fekete points. Extensive computations for optimal configurations and their corresponding extremal energies have been reported in a number of articles. Most deal with the Coulomb case ($t = 1$) [33,34]. It has been observed that for a large N there are many local minima in the energy minimization problem. Further, these local minima have energies very close to the global minimum, which makes it very difficult to determine the precise minimum.

In this work, the Fekete points over S^3 were estimated using gradient descent. The basic idea comes from electrostatics, which dictates how the charged particles over the surface of a sphere (hypersphere) can move to reach a configuration ω_N with minimum potential energy (or very close to it) along with static stable equilibrium. The repulsive force F, which is the negative of the potential gradient $(-\nabla U)$ is calculated on each particle due to the influence of the rest. In every iteration, particles are moved in the direction d to reduce the net U of the system.

$$\omega_N^{i+1} = \omega_N^i + \beta d \tag{16}$$

$$d = (F_1^{\mathrm{T}}, F_2^{\mathrm{T}}, \ldots, F_N^{\mathrm{T}}) \tag{17}$$

where F_i^{T} is the tangential component of force acting on the ith particle due to the rest of the particles, and β is a constant controlling the amount of displacement for the particles. The antipodal symmetry introduced in the initialization was kept intact during the gradient descent by tying the antipodal points together and moving them in pairs. A distribution based on UF4 in shown in Fig. 1d.

After accounting for the EPRI related constraints, the energy U and the standard deviation of the Voronoi cell size [35] are calculated for all four sampling patterns and are shown in Fig. 2. The computation of Voronoi cells, also used to assign relative weight to each projection before applying the FBP, over S^3 is similar to a previously reported procedure for S^2 [17].

2.5. Missing angle problem and single-stage reconstruction

For spectral-spatial imaging, $\theta = 90^\circ$ corresponds to acquiring projection data at an infinite magnetic field gradient strength. Since hardware limitations and SNR put a restriction on the maximum applicable gradient, the projection data corresponding to higher gradients cannot be acquired. If θ_{m} is the missing angle

$$\theta_{\mathrm{m}} = 90^\circ - \theta_{\max} \tag{18}$$

$$\theta_{\max} \leqslant \theta_G = \tan^{-1}\left(|G_{\max}| \frac{\Delta L}{\Delta B}\right) \tag{19}$$

where θ_G is the spectral angle associated with the maximum applicable gradient strength $G_{\max}$ and $\theta_{\max}$ is the spectral angle corresponding the maximum gradient reached by a sampling method.

This problem is generally termed as "missing angle tomography." Although there are alternative reconstruction techniques [36] that can handle this problem seamlessly, the computation cost associated with such techniques especially for 4D render them impractical. For FBP, a few techniques such as projection–reprojection [37] have been proposed to handle this problem. Therefore, one simple solution would be to estimate the Fekete distribution

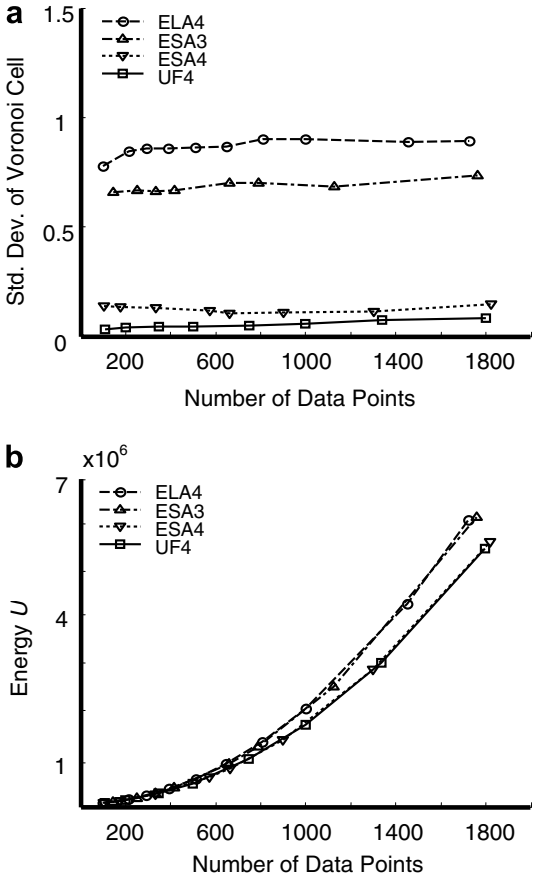

Fig. 2. (a) Standard deviation of the Voronoi cell size drawn on the surface of S^3 for different number of data points. (b) Extremal energy U for various distributions.

over S^3, remove the data points appearing in the "forbidden" region, and perform the reconstruction using projection–reprojection. The resulting reconstruction, however, yields poor resolution since there are an insufficient number of high gradient projections that are vital for the reconstruction quality.

In this work, the missing angle problem is tackled by introducing a slight discrepancy in the distribution of data along the spectral angle. For all methods except UF4, the spectral angle sampling interval $\Delta\theta$ is chosen such that the missing angle region around $\theta = 90°$ is avoided altogether. On the other hand, for UF4, where there is no fixed sampling interval, the discrepancy is only locally introduced during the iterative process to generate Fekete points. In each iteration, points appearing in the region $\theta_{\max} \pm \theta_{\mathrm{m}}$ are set equal to $\theta_{\max}$, and points appearing in the region $180° - \theta_{\max} \pm \theta_{\mathrm{m}}$ are set equal to $180° - \theta_{\max}$. Although the introduced discrepancy may degrade the reconstruction quality, our experience with the simulation data shows that this technique is considerable superior to the projection–reprojection technique because in this case we have a large number of projections acquired at the maximum gradient strength. Further, for UF4 the loss of reconstruction quality due to the adjustments made in the data distribution is far less pronounced than it is for ELA4, ESA3, or ESA4. This is because the adjustments for UF4 are restricted to the $90° \pm 2\theta_{\mathrm{m}}$ region, while for ELA4, ESA3, and ESA4 the effect of the adjustment made to tackle the missing angle problem trickle down the entire distribution. More importantly, for ELA4, ESA3, and ESA4, the calculated step size $\Delta\theta$ for a given number of projections may be considerably greater than $2\theta_{\mathrm{m}}$. Therefore, the resulting $\theta_{\max} = \theta_G - (\Delta\theta/2 - \theta_{\mathrm{m}})$ can be considerably lesser than θ_G, which would expand the missing angle region beyond the limits imposed by the hardware or SNR. For UF4, the equality $\theta_{\max} = \theta_G$ can be attained for any number of projections.

All calculations were performed using Matlab 7.0 (MathWorks, Massachusetts) on a Pentium IV computer equipped with 1 GB RAM and 3.2 GHz of clock speed. For a $64 \times 64 \times 64 \times 64$ reconstruction from 1000 projections, with each projection having a size of 95 points, the approximate computation times are: Radon transform: 18 min, inverse Radon transform: 82 min, and nonlinear least-square fitting at each voxel using Matlab command *lsqnonlin*: 90 ms. The projection acquisition process was carried out in multiple stages using partial Radon transform [38] to reduce the computation time. For single-stage reconstruction, four matrices X, Y, Z, and S, each of size $64 \times 64 \times 64 \times 64$ were generated and plugged in the reconstruction equation to directly calculate $\tilde{f}(x, y, z, s)$. The large sizes of the matrices posed a serious limitation on the computer memory. To avoid this problem each of the four matrices were divided into two halves The resulting 16 subsets of the reconstruction space were reconstructed one by one and then put together to generate the final image without scarifying any reconstruction quality. Since both the FBP and curve-fitting are easy to parallelize, using multiple processor nodes to further speed up the reconstruction is a viable option.

3. Results

3.1. Simulations

To demonstrate the performance of 4D uniform sampling, the reconstruction results from the four acquisition techniques are compared using a digital phantom of size $64 \times 64 \times 64 \times 64$. The phantom consists of four rows and four columns of cylindrical tubes as shown in Fig. 3a. Two different intensities and linewidths are used in the phantom. The outer 12 tubes simulate a normalized intensity of 1 and a peak-to-peak linewidth of 0.27 G while the central 4 tubes simulate a normalized intensity of 0.7 and a peak-to-peak linewidth of 0.18 G. The imaging parameters, chosen to simulate EPRI experiments at L-band (1.2 GHz), were as follows: spatial FOV ΔL: sphere inscribed in $2 \times 2 \times 2$ cm^3 cube, spectral window ΔB: 2.5 G, data points per projection: 95, maximum gradient strength: 12 G/cm ($\theta_G = 84°$), scan speed: 1.85 G/s. To partially suppress noise at high gradient strengths, acquisition time for each projection was made proportional to $\Delta B/\cos\theta$. After

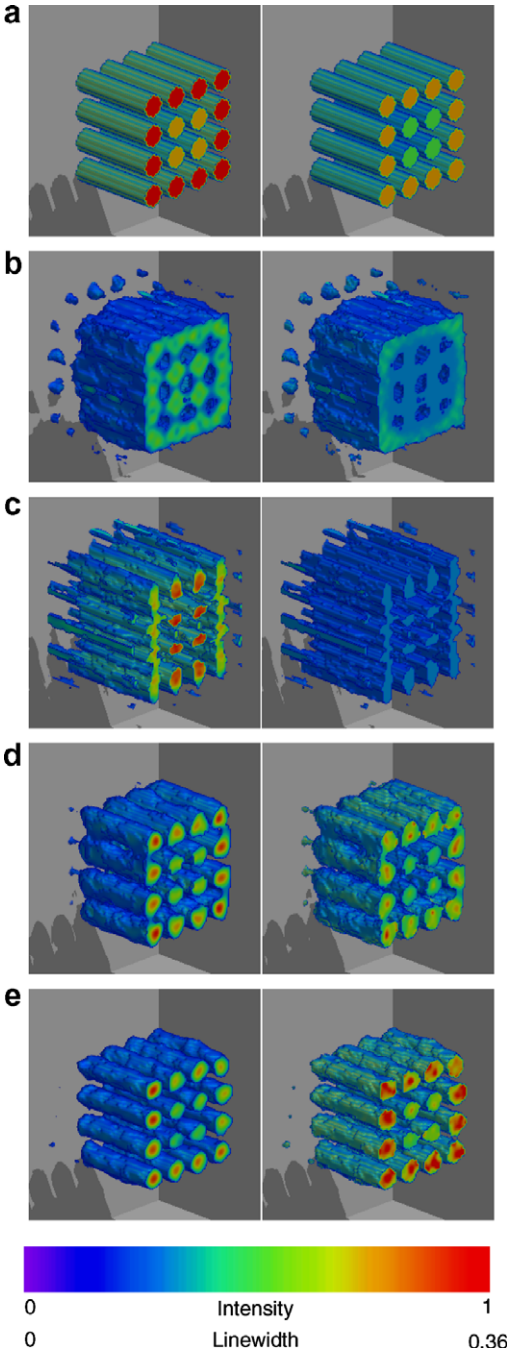

Fig. 3. Simulation results displaying the reconstructions based on the different sampling patterns. The first column represents spin density (obtained by integrating the 4D object along the spectral axis) while the second column represents peak-to-peak linewidth at each spatial location given in the first column. (a) A simulated phantom consisting of 16 tubes with two different linewidths and spin densities. The normalized spin densities for outer 12 and inner 4 tubes are 1.0 and 0.7, respectively, and the linewidths for outer 12 and inner 4 tubes are 0.27 and 0.18 G, respectively. (b) Reconstruction based on 1000 projections collected by ELA4. (c) Reconstruction based on 948 projections collected by ESA3. (d) Reconstruction from 664 projections acquired using ESA4. (e) Reconstruction from 605 projections acquired using UF4.

partial suppression, the additive noise was assumed to be white Gaussian with intensity proportional to $1/\cos\theta$. The SNR, defined as the ratio of peak signal amplitude (for the projection with minimum peak-to-peak amplitude) and standard deviation of the additive white noise, was 30. The total number of projections and the corresponding acquisition time for each sampling technique is given in Table 1. Fig. 3 shows the reconstructed images from the four sampling techniques.

Table 1
Number of projections for each acquisition technique and corresponding acquisition time for the simulation and experimental data

	ELA4	ESA3	ESA4	UF4
Simulation				
Number of projections	1000	948	664	605
θ_{max}	81°	82.4°	82.5°	84°
Number of projections corresponding to θ_{max}	188	158	219	162
Acquisition time (min)	84	85	83	84
Experiment				
Number of projections	1728	1512	1036	1000
θ_{max}	82.5°	82.5°	83.6°	84.3°
Number of projections corresponding to θ_{max}	288	252	290	259
Acquisition time (min)	190	175	175	160

Here, θ_{max} is the maximum gradient angle achieved by the sampling pattern.

3.2. EPRI experiment

An experimental phantom as shown in Fig. 4 was constructed using eighteen 100 μL capillary tubes. The capillary tubes were arranged in three columns with each column containing six capillaries. Two different triarylmethyl free radical (TAM) probes were used. TAM in aqueous solution exhibits a single narrow EPR spectrum which is suitable for imaging purposes. Twelve capillaries, constituting the 1st and 3rd columns, were filled with 2 mM Ox063 (methyl-tris[8-carboxy-2,2,6,6-tetrakis[2-hydroxyethyl]benzo[1,2-d;4,5-d′]bis[1,3]dithiol-4-yl]-, trisodium salt, MW 1427) while six capillaries in the middle column were filled with 1 mM Ox031 (methyl-tris[8-carboxy-2,2,6,6-tetrakis[(2-hydroxyethoxy)methyl]benzo[1,2-d:4,5-d′]bis[1,3]-dithiol-4-yl]-, trisodium salt, MW 1787.1) up to a height of

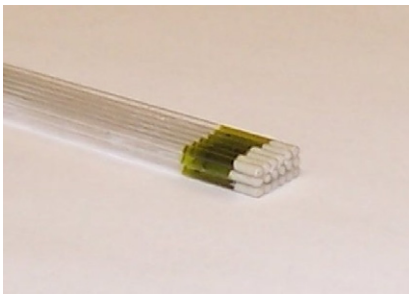

Fig. 4. The phantom used to obtain the experimental data. There are a total of 18 capillaries arranged on a 6×3 grid. True normalized spin densities for two outer columns (1st and 3rd) and middle column (2nd) are 1.0 and 0.67, respectively, and the linewidths for two outer columns (1st and 3rd) and middle column (2nd) are 0.25 and 0.18 G, respectively.

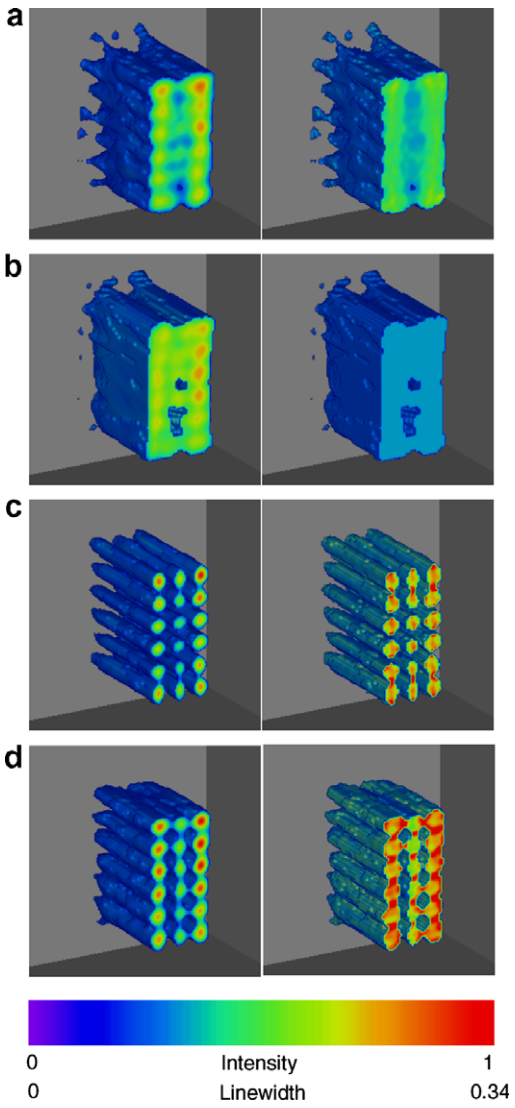

Fig. 5. Experimental results displaying the reconstructions based on the different sampling patterns. The first column represents spin density (obtained by integrating the 4D object along the spectral axis) while the second column represents peak-to-peak linewidth at each spatial location given in the first column. (a) Reconstruction based on 1728 projections collected by ELA4. (b) Reconstructed based on 1512 projections collected by ESA3. (c) Reconstruction from 1036 projections acquired using ESA4. (d) Reconstruction from 1000 projections acquired using UF4.

10 mm. For Ox063 and Ox031, the respective room air peak-to-peak linewidths, measured at X-band, were 0.25 and 0.18 G while the signal intensities were approximately 3:2. The overall sample dimensions were $10.2 \times 10 \times 5.2\ \text{mm}^3$.

The phantom was imaged using an L-Band (1.2 GHz) EPRI system with a reentrant resonator with cylindrical sample volume with a diameter of 12.6 mm and useable height of 12 mm. The spectrometer settings were: incident microwave power: 4 mW, spectral window ΔB: 1.8 G, spatial FOV ΔL: sphere inscribed by $1.8 \times 1.8 \times 1.8\ \text{cm}^3$ cube, modulation amplitude: 70 mG, maximum gradient strength: 10 G/cm ($\theta_G = 84.3°$), time constant of lock-in amplifier: 20 ms. A total of four datasets (one for each sampling method) were acquired. The number of projections and the acquisition time for each dataset are reported in Table 1. For each projection 1024 data points were collected which were later downsampled to 95 for faster reconstruction. No correction for B_1 field inhomogeneities was applied. To suppress noise for high gradient projections, the acquisition time for each projection was made proportional to $\Delta B/\cos\theta$ which implies that the scan speed across all projections was kept constant at 1.38 G/s. The measured SNR was 12. The measured lineshapes for both Ox031 and Ox063 were reasonable approximations of a Lorentzian function with fit error <7%. Fig. 5 displays the reconstructed images from the four acquisition techniques.

4. Discussion

The simulation and experimental results suggest that the distribution of projection data contributes to the reconstruction quality. The distributions which are more uniform tend to capture more distinct information in each projection which results in high fidelity images that possess more information about the object. ELA4 and ESA3-based distributions repeat the same spatial distribution of gradient directions for each spectral angle which results in enhanced redundancy in the acquired data. In addition, if any edge of the object gets aligned with the sampling pattern, the streak-artifact from the edge may get added constructively that can consequently degrade the image quality.

Fig. 2a displays the standard deviation of the Voronoi cell size for the four distributions with UF4 exhibiting considerably lower variations in the Voronoi cell size which is also used to find proper weighting for the acquired projections before performing the FBP. The energy U associated with the distributions is displayed in Fig. 2b. Among all the distributions, UF4 and ELA4 possess the minimum and maximum value of U, respectively.

The simulation results are presented in Fig. 3. The quantification of the results is provided in Table 2. Since the FBP-based reconstruction from a limited number of projections generate strong background artifacts, the voxels reflecting a spin density (obtained by integration of 4D object along spectral axis) less than 25% of the maximum spin density were set to zero to make for a better 3D visualization. However, caution should be observed in applications where voxels with weak and strong spin densities coexist in a single object because discarding the part of such an object based on the intensity may result in loss of important information. To quantify the linewidth, data at each voxel were fit with a Lorentzian function with allowable linewidth of $0.7\text{LW}_{\text{min}}$ to $1.3\text{LW}_{\text{max}}$. Here, LW_{min} and LW_{max} are the minimum and maximum linewidths, respectively, present in the sample. The quantification of spin densities and linewidths was done for all the voxels where spin density of the input phantom was nonzero. For better visualization of the parameters, input

Table 2
Quantification of simulation and experimental results

	ELA4	ESA3	ESA4	UF4
Simulation				
Mean intensity of outer 12 tubes	0.789 (±0.162)	0.791 (±0.099)	1.000 (±0.229)	1.000 (±0.223)
Mean intensity of inner 4 tubes	1.000 (±0.220)	1.000 (±0.050)	0.740 (±0.130)	0.704 (±0.132)
Mean linewidth of outer 12 tubes	0.126 (±0.011)	0.113 (±0.002)	0.229 (±0.045)	0.284 (±0.038)
Mean linewidth of inner 4 tubes	0.113 (±0.000)	0.112 (±0.000)	0.152 (±0.018)	0.201 (±0.024)
Experiment				
Mean intensity of 1st and 3rd column	1.000 (±0.284)	1.000 (±0.202)	1.000 (±0.279)	1.000 (±0.261)
Mean intensity of 2nd column	0.694 (±0.187)	0.948 (±0.156)	0.774 (±0.178)	0.704 (±0.154)
Mean linewidth 1st and 3rd column	0.163 (±0.017)	0.114 (±0.002)	0.243 (±0.032)	0.257 (±0.033)
Mean linewidth of 2nd column	0.125 (±0.008)	0.113 (±0.000)	0.234 (±0.038)	0.207 (±0.034)

For simulations, true normalized spin densities for outer 12 and inner 4 tubes are 1.0 and 0.7, respectively, and the true linewidths for outer 12 and inner 4 tubes are 0.27 and 0.18 G, respectively. For experimental data, true normalized spin densities for two outer columns (1st and 3rd) and middle column (2nd) are 1.0 and 0.67, respectively, and the linewidths for two outer columns (1st and 3rd) and middle column (2nd) are 0.25 and 0.18 G, respectively.

and reconstructed images were cropped 33% along the axis of tubes.

For ELA4 and ESA3, a fixed sampling interval along θ, which is decided by the total number of projections to be acquired, restricts us from applying the maximum permissible gradient, which translates to a lower resolution. It is this inability of ELA4 and ESA3 to utilize the maximum gradient allowed by the hardware along with the relatively lesser number of high gradient projections that has resulted in extremely poor resolution for objects with fine spatial structures like the ones used in this work. For the simulation results shown in Fig. 3, value of $\theta_{\max}$ and the corresponding number of projections are given in Table 1. Further, since the distribution of the data is structured, the reconstruction is sensitive to the alignment of the sampling grid and the distribution of information content. Therefore, the reconstruction may possess an orientational bias, and rotating the object for a given sampling may change the reconstruction quality considerably [17]. As a result, the reconstruction quality may vary with the number of acquired projections, configuration of the object to be imaged, and the orientation of the sampling grid relative to the phantom. On the other hand, the improved uniformity of ESA4 and especially of UF4 ensures that the results are relatively insensitive to the object content [27]. By our simulation experience (results not shown), we have further observed that for objects which lack fine structure, the difference in the reconstruction quality of uniform and non-uniform sampling patterns may not be that drastic because high gradient data may not carry same importance for such objects. Finally, for UF4 it is possible to acquire any number of projections, while for other three methods there are only discrete values that can be acquired.

The experimental results provided in Fig. 5 and Table 2 are consistent with the simulation findings. Since ESA4 seems to resolve all the 18 tubes, the nonzero voxels in ESA4 based reconstruction are used to define the true spatial structure of the phantom. Hence for quantifying the reconstruction results of all the four sampling patterns, the spin densities and linewidths only at these nonzero voxels are taken into consideration.

5. Conclusions

The uniform coverage of 4D space is important for an improved reconstruction quality. A poor approximation of the uniform distribution, on the other hand, may result in pronounced artifacts in the reconstructed image which can degrade the reconstruction quality to an unacceptable level. Although data distribution based on ESA3 provides an improvement over ELA4, it is still not uniform in the 4D acquisition space. The distributions based on ESA4 and especially UF4 provide a tangible improvement over ELA4 and ESA3. Besides, by breaking down the reconstruction into subsets, single-stage reconstruction can be realized without special computing resources. Since computation time for the single-stage backprojection is comparable to the acquisition time, real time reconstruction is also feasible.

Acknowledgment

This work was supported by NIH Grant EB005004.

Appendix A

A.1. Fourier Slice Theorem in 4D

$$\begin{aligned}&\text{If } \vec{c} = [\cos\eta\sin\phi\sin\theta \quad \sin\eta\sin\phi\sin\theta \quad \cos\phi\sin\theta \quad \cos\theta]^{\mathrm{T}}\\ &\vec{k} = [k_x \quad k_y \quad k_z \quad k_s]^{\mathrm{T}}\\ &\vec{r} = [x \quad y \quad z \quad s]^{\mathrm{T}}\end{aligned} \tag{A1}$$

for a 4D object $f(\vec{r})$, the Fourier transform $F(\vec{k})$ can be written as

$$F(\vec{k}) = \int_{-\infty}^{\infty}\int_{-\infty}^{\infty}\int_{-\infty}^{\infty}\int_{-\infty}^{\infty} f(\vec{r})\cdot \mathrm{e}^{-j2\pi(\vec{k}\cdot\vec{r})}\mathrm{d}x\mathrm{d}y\mathrm{d}z\mathrm{d}s \tag{A2}$$

where $\vec{k}\cdot\vec{r}$ is the inner product of the two vectors. If v represents the radial distance from the center of $F(\vec{k})$ and ρ defines the distance in $\vec{r}$ of a particular line of integration from the origin then for a line $\vec{k}=v\vec{c}$

$$\begin{aligned}F(v\vec{c}) &= \int_{-\infty}^{\infty}\int_{-\infty}^{\infty}\int_{-\infty}^{\infty}\int_{-\infty}^{\infty}\int_{-\infty}^{\infty} f(\vec{r})\delta(\rho-\vec{c}\cdot\vec{r})\mathrm{d}x\mathrm{d}y\mathrm{d}z\mathrm{d}s \\ &\quad\cdot \mathrm{e}^{-j2\pi v\rho}\mathrm{d}\rho \\ &= \int_{-\infty}^{\infty}\underbrace{\int_{-\infty}^{\infty}\int_{-\infty}^{\infty}\int_{-\infty}^{\infty}\int_{-\infty}^{\infty} f(\vec{r})\delta(\rho-\vec{c}\cdot\vec{r})\mathrm{d}x\mathrm{d}y\mathrm{d}z\mathrm{d}s}_{\text{projection}}\cdot\mathrm{e}^{-j2\pi v\rho}\mathrm{d}\rho\end{aligned} \tag{A3}$$

$$\begin{aligned}F(v\vec{c}) &= \int_{-\infty}^{\infty} p(\rho,\eta,\phi,\theta)\cdot\mathrm{e}^{-j2\pi v\rho}\mathrm{d}\rho \\ &= \mathrm{FT}[p(\rho,\eta,\phi,\theta)]\end{aligned} \tag{A4}$$

A.2. Filtered backprojection in 4D

Inverse Fourier transform in 4D

$$f(\vec{r}) = \int_{-\infty}^{\infty}\int_{-\infty}^{\infty}\int_{-\infty}^{\infty}\int_{-\infty}^{\infty} F(\vec{k})\cdot\mathrm{e}^{j2\pi(\vec{k}\cdot\vec{r})}\mathrm{d}k_x\mathrm{d}k_y\mathrm{d}k_z\mathrm{d}k_s \tag{A5}$$

which can be also written in hyperspherical coordinate system that can be easily computed from the determinant of the Jacobian matrix $\partial(k_x,k_y,k_z,k_s)/\partial(v,\eta,\phi,\theta)$

$$\begin{aligned}f(\vec{r}) &= \int_0^{\pi}\int_0^{\pi}\int_0^{2\pi}\int_0^{\infty} F(v\vec{c})\cdot\mathrm{e}^{j2\pi(v\vec{c}\cdot\vec{r})}\cdot v^3\sin\phi\sin^2\theta\mathrm{d}v\mathrm{d}\eta\mathrm{d}\phi\mathrm{d}\theta \\ f(\vec{r}) &= \int_0^{\pi}\int_0^{\pi}\int_0^{\pi}\int_0^{\infty} F(v\vec{c})\cdot\mathrm{e}^{j2\pi v(\vec{c}\cdot\vec{r})}\cdot v^3\sin\phi\sin^2\theta\mathrm{d}v\mathrm{d}\eta\mathrm{d}\phi\mathrm{d}\theta \\ &\quad+\int_0^{\pi}\int_0^{\pi}\int_{\pi}^{2\pi}\int_0^{\infty} F(v\vec{c})\cdot\mathrm{e}^{j2\pi v(\vec{c}\cdot\vec{r})}\cdot v^3\sin\phi\sin^2\theta\mathrm{d}v\mathrm{d}\eta\mathrm{d}\phi\mathrm{d}\theta\end{aligned} \tag{A6}$$

which after some manipulation can be written as

$$\begin{aligned}f(\vec{r}) &= \int_0^{\pi}\int_0^{\pi}\int_0^{\pi}\int_0^{\infty} F(v\vec{c})\cdot\mathrm{e}^{j2\pi v(\vec{c}\cdot\vec{r})}v^3 \\ &\quad\times\sin\phi\sin^2\theta\mathrm{d}v\mathrm{d}\eta\mathrm{d}\phi\mathrm{d}\theta+\int_0^{\pi}\int_0^{\pi}\int_0^{\pi} \\ &\quad\times\int_{-\infty}^{0} F(v\vec{c})\cdot\mathrm{e}^{j2\pi v(\vec{c}\cdot\vec{r})}(-v^3) \\ &\quad\times\sin\phi\sin^2\theta\mathrm{d}v\mathrm{d}\eta\mathrm{d}\phi\mathrm{d}\theta\end{aligned} \tag{A7}$$

Therefore,

$$\begin{aligned}f(\vec{r}) &= \int_0^{\pi}\int_0^{\pi}\int_0^{\pi}\int_{-\infty}^{\infty}\underbrace{|v|^3}_{\text{filter}} F(v\vec{c})\cdot\mathrm{e}^{j2\pi v(\vec{c}\cdot\vec{r})} \\ &\quad\times\sin\phi\sin^2\theta\mathrm{d}v\mathrm{d}\eta\mathrm{d}\phi\mathrm{d}\theta\end{aligned} \tag{A8}$$

From Eqs. (A4) and (A8)

$$f(\vec{r}) = \int_0^{\pi}\int_0^{\pi}\int_0^{\pi}\underbrace{\int_{-\infty}^{\infty}|v|^3\int_{-\infty}^{\infty} p(\tilde{\rho},\eta,\phi,\theta)\cdot\mathrm{e}^{-j2\pi v\tilde{\rho}}\mathrm{d}\tilde{\rho}\cdot\mathrm{e}^{j2\pi v\rho}\mathrm{d}v}_{\text{filtered projection } p_{\mathrm{f}} \text{ in spatial domain}}\sin\phi\sin^2\theta\mathrm{d}\eta\mathrm{d}\phi\mathrm{d}\theta \tag{A9}$$

$$f(\vec{r}) = \int_0^{\pi}\int_0^{\pi}\int_0^{\pi} p_{\mathrm{f}}(\vec{c}\cdot\vec{r},\eta,\phi,\theta)\sin\phi\sin^2\theta\mathrm{d}\eta\mathrm{d}\phi\mathrm{d}\theta \tag{A10}$$

or equivalently,

$$\begin{aligned}f(\vec{r}) &= \int_0^{\pi}\int_0^{\pi}\int_0^{\pi}\int_{-\infty}^{\infty} p_{\mathrm{f}}(\rho,\eta,\phi,\theta)\cdot\delta(\rho-\vec{c}\cdot\vec{r}) \\ &\quad\times\sin\phi\sin^2\theta\mathrm{d}\rho\mathrm{d}\eta\mathrm{d}\phi\mathrm{d}\theta\end{aligned} \tag{A11}$$

References

[1] M. Ferrari, V. Quaresima, A. Sotgiu, Present status of electron paramagnetic resonance (EPR) spectroscopy/imaging for free radical detection, Pflugers Arch. 431 (1996) R267–R268.

[2] H. Fujii, L.J. Berliner, One- and two-dimensional EPR imaging studies on phantoms and plant specimens, Magn. Reson. Med. 2 (1985) 275–282.

[3] J. Fuchs, H.J. Freisleben, N. Groth, T. Herrling, G. Zimmer, R. Milbradt, L. Packer, One- and two-dimensional electron paramagnetic resonance imaging in skin, Free Radic. Res. Commun. 15 (1991) 245–253.

[4] P. Kuppusamy, EPR spectroscopy in biology and medicine, Antioxid. Redox Signal 6 (2004) 583–585.

[5] A. Matsumoto, S. Matsumoto, A.L. Sowers, J.W. Koscielniak, N.J. Trigg, P. Kuppusamy, J.B. Mitchell, S. Subramanian, M.C. Krishna, K. Matsumoto, Absolute oxygen tension (pO(2)) in murine fatty and muscle tissue as determined by EPR, Magn. Reson. Med. 54 (2005) 1530–1535.

[6] E.L. Rolett, A. Azzawi, K.J. Liu, M.N. Yongbi, H.M. Swartz, J.F. Dunn, Critical oxygen tension in rat brain a combined (31)P-NMR and EPR oximetry study, Am. J. Physiol. Regul. Integr. Comp. Physiol. 279 (2000) R9–R16.

[7] B.B. Williams, H. al Hallaq, G.V. Chandramouli, E.D. Barth, J.N. Rivers, M. Lewis, V.E. Galtsev, G.S. Karczmar, H.J. Halpern, Imaging spin probe distribution in the tumor of a living mouse with 250 MHz EPR: correlation with BOLD MRI, Magn. Reson. Med. 47 (2002) 634–638.

[8] Y. Deng, P. Kuppusamy, J.L. Zweier, Progressive EPR imaging with adaptive projection acquisition, J. Magn. Reson. 174 (2005) 177–187.

[9] J. Bourg, M.C. Krishna, J.B. Mitchell, R.G. Tschudin, T.J. Pohida, W.S. Friauf, P.D. Smith, J. Metcalfe, F. Harrington, S. Subramanian, Radiofrequency FT EPR spectroscopy and imaging, J. Magn. Reson. B 102 (1993) 112–115.

[10] S.R. Deans, The Radon Transform and Some of its Applications, Wiley, New York, 1983.

[11] L.A. Shepp, B.F. Logan, The Fourier reconstruction of a head section, IEEE Trans. Nucl. Sci. 21 (1974) 21–42.

[12] Z.H. Cho, J.P. Jones, M. Singh, Foundations of Medical Imaging, Wiley, New York, 1993.

[13] P. Kuppusamy, M. Chzhan, J.L. Zweier, Development and optimization of three-dimensional spatial EPR imaging for biological organs and tissues, J. Magn. Reson. B 106 (1995) 122–130.

[14] S.S. Maltempo, S.S. Eaton, G.R. Eaton, Spectral-spatial two-dimensional EPR imaging, J. Magn. Reson. 72 (1987) 449–455.

[15] P. Kuppusamy, R.A. Shankar, J.L. Zweier, In vivo measurement of arterial and venous oxygenation in the rat using 3D spectral-spatial electron paramagnetic resonance imaging, Phys. Med. Biol. 43 (1998) 1837–1844.

[16] G. Placidi, M. Alecci, A. Sotgiu, Theory of adaptive acquisition method for image reconstruction from projections and application to EPR imaging, J. Magn. Reson. 108 (1995) 55–57.

[17] R. Ahmad, Y. Deng, D.S. Vikram, B. Clymer, P. Srinivasan, J.L. Zweier, P. Kuppusamy, Quasi Monte Carlo-based isotropic distribution of gradient directions for improved reconstruction quality of 3D EPR imaging, J. Magn. Reson. 184 (2007) 236–245.

[18] K.H. Ahn, H.J. Halpern, Spatially uniform sampling in 4-D EPR spectral-spatial imaging, J. Magn. Reson. (2006).
[19] C.M. Lai, P.C. Lauterbur, A gradient control device for complete three-dimensional nuclear magnetic resonance zeugmatographic imaging, J. Phys. E: Sci. Instrum. 13 (1980).
[20] E.B. Saff, A.B. Kuijlaars, Distributing many points on a sphere, Math. Intelligencer 10 (1997) 5–11.
[21] P. Kuppusamy, M. Chzhan, A. Samouilov, P. Wang, J.L. Zweier, Mapping the spin-density and lineshape distribution of free radicals using 4D spectral-spatial EPR imaging, J. Magn. Reson. B 107 (1995) 116–125.
[22] E. Hlawka, Funktionen von beschränkter Variation in der Theorie der Gleichverteilung, Annali di Matematica Pura ed Applicata 54 (1961) 325–333.
[23] J.R. Morris, D.M. Deaven, K.M. Ho, Genetic-algorithm energy minimization for point charge on a sphere, Phys. Rev. B 53 (1996).
[24] A. Katanforoush, M. Shahshahani, Distributing Points on the Sphere, I. Exp. Math. 12 (2003) 199–209.
[25] J.H. Hannay, J.F. Nye, Fibonacci numerical integration on a sphere, J. Phys. A: Math. Gen. 37 (2004) 11591–11601.
[26] D.W. Alderman, M.S. Solum, D.M. Grant, Methods for analyzing spectroscopic line shapes. NMR solid powder patterns, J. Chem. Phys. 84 (1986) 3717–3725.
[27] M. Bak, N.C. Nielsen, REPULSION, a novel approach to efficient powder averaging in solid-state NMR, J. Magn. Reson. 125 (1997) 132–139.
[28] R.H. Hardin, N.J.A. Sloane, New spherical 4-designs, Discrete Math. 106/107 (1992) 255–264.
[29] E.A. Rakhmanov, E.B. Saff, Y.M. Zhou, Minimal discrete energy on the sphere, Math. Res. Lett. 1 (1994) 647–662.
[30] P. Shirley, Discrepancy as a quality measure for sample distributions, Proc. Eurographics 91 North-Holland, 1991, pp. 183–193.
[31] S.B. Damelin, P.J. Grabner, Energy functionals numerical integration and asymptotic equidistribution on the sphere, J. Complexity 19 (2003) 231–246.
[32] S.B. Damelin, V. Maymeskul, On point energies separation radius and mesh norm for s-extremal configurations on compact sets in Rn, J. Complexity 21 (2005) 845–863.
[33] T. Erber, G.M. Hockney, Equilibrium configurations of N equal charges on a sphere, J. Phys. A: Math. Gen. 24 (1991) L1369–L1377.
[34] L. Glasser, A.G. Every, Energies and spacings of point charges on a sphere, J. Phys. A: Math. Gen. 25 (1992) 2473–2482.
[35] H.S. Na, C.N. Lee, O. Cheong, Voronoi diagrams on the sphere, Comput. Geom.: Theory Appl. 23 (2002) 183–194.
[36] M. Tseitlin, A. Dhami, S.S. Eaton, G.R. Eaton, Comparison of maximum entropy and filtered back-projection methods to reconstruct rapid-scan EPR images, J. Magn. Reson. 184 (2007) 157–168.
[37] A.E. Stillman, D.N. Levin, Back projection reconstruction of spectroscopic NMR images from incomplete sets of projections, J. Magn. Reson. 69 (1986) 168–175.
[38] L. Zhi-Pei, D.C.J. Munson, Partial Radon transforms, IEEE Trans. Imag. Proc. 6 (1997) 1467–1469.